

Quantitative pulsed CEST-MRI using Ω -plots

Jan-Eric Meissner^{a,b,*}, Steffen Goerke^a, Eugenia Rerich^a, Karel D. Klika^c, Alexander Radbruch^{b,d}, Mark E. Ladd^a, Peter Bachert^a and Moritz Zaiss^a



Chemical exchange saturation transfer (CEST) allows the indirect detection of dilute metabolites in living tissue via MRI of the tissue water signal. Selective radio frequency (RF) with amplitude B_1 is used to saturate the magnetization of protons of exchanging groups, which transfer the saturation to the abundant water pool. In a clinical setup, the saturation scheme is limited to a series of short pulses to follow regulation of the specific absorption rate (SAR). Pulsed saturation is difficult to describe theoretically, thus rendering quantitative CEST a challenging task. In this study, we propose a new analytical treatment of pulsed CEST by extending a former interleaved saturation-relaxation approach. Analytical integration of the continuous wave (cw) eigenvalue as a function of the RF pulse shape leads to a formula for pulsed CEST that has the same structure as that for cw CEST, but incorporates two form factors that are determined by the pulse shape. This enables analytical Z-spectrum calculations and permits deeper insight into pulsed CEST. Furthermore, it extends Dixon's Ω -plot method to the case of pulsed saturation, yielding separately, and independently, the exchange rate and the relative proton concentration. Consequently, knowledge of the form factors allows a direct comparison of the effect of the strength and B_1 dispersion of pulsed CEST experiments with the ideal case of cw saturation. The extended pulsed CEST quantification approach was verified using creatine phantoms measured on a 7 T whole-body MR tomograph, and its range of validity was assessed by simulations. Copyright © 2015 John Wiley & Sons, Ltd.

Additional supporting information may be found in the online version of this article at the publisher's web site.

Keywords: CEST; Ω -plot; pulsed pre-saturation; creatine; MRI

INTRODUCTION

Chemical exchange saturation transfer (CEST) has emerged as a promising MRI contrast enabling the detection of proton species of low concentration in living tissue (1,2). The CEST effects of protons in endogenous macromolecules such as proteins (3) and in metabolites of small molecular mass such as creatine (4) and glucose (5), as well as administered paramagnetic CEST (PARACEST) (6) and diamagnetic CEST agents (7), have all been reported. In addition to concentration, correlations with pH were also reported, thus promising the possibility of highly resolved pH mapping *in vivo* using amide or amine protons (3,8–10). A quantitative CEST data evaluation approach with access to concentration and pH, i.e. a quantitative CEST signal as already proposed by other groups (11–14), would be of high interest. pH and concentration maps *in vivo* could offer insights in the pathophysiology of stroke (15) or oncologic diseases such as brain tumors (16–18) and thus help to improve guidance for resection or radiotherapy. Another potentially interesting application comes via the creatine concentration, which correlates with the energy metabolism of healthy and pathological tissue (4,19). This allows for comparison using the CEST effect of creatine.

However, this emerging CEST contrast, as it is dependent on several technical and physiological variables, is very complex, especially for human applications. The variables include the following: (i) the exchange rate k_{BA} , which is dependent on the pH and the relative concentration of the rare species f_B that appear as a product in the formula of the ideal CEST effect (11,20,21); (ii) the ideal CEST effect is altered by water relaxation properties, which in turn depend on the tissue type, the so called spillover effect (21,22); (iii) the trains of shaped

pulses used on clinical tomographs, which are maintained within specific absorption rate (SAR) and solid-state amplifier limits (23,24).

* Correspondence to: Jan-Eric Meissner, Division of Medical Physics in Radiology, Deutsches Krebsforschungszentrum (DKFZ) [German Cancer Research Center], Heidelberg, Germany.
E-mail: j.meissner@dkfz-heidelberg.de

a J.-E. Meissner, S. Goerke, E. Rerich, M. E. Ladd, P. Bachert, M. Zaiss
Division of Medical Physics in Radiology, Deutsches Krebsforschungszentrum (DKFZ) [German Cancer Research Center], Heidelberg, Germany

b J.-E. Meissner, A. Radbruch
Division of Radiology, Deutsches Krebsforschungszentrum (DKFZ) [German Cancer Research Center], Heidelberg, Germany

c K. D. Klika
Molecular Structure Analysis, Deutsches Krebsforschungszentrum (DKFZ) [German Cancer Research Center], Heidelberg, Germany

d A. Radbruch
Department of Neuroradiology, Medical Faculty, University of Heidelberg, Heidelberg, Germany

Abbreviations used: AREG, apparent exchange-dependent relaxation; $AREX_{cw}$, AREG in the case of continuous wave pre-saturation; $AREX_{pulsed}$, AREG in the case of pulsed pre-saturation; BM, Bloch–McConnell; CERT, chemical exchange rotation transfer; CEST, chemical exchange saturation transfer; CW, continuous wave; DC, duty cycle; FoV, field of view; Gd, gadolinium; GRE, gradient echo; MT, semi-solid magnetization transfer; MTR_{Relax} , magnetization transfer ratio yielding R_{ex} ; PARACEST, paramagnetic CEST; QUESP, quantification of exchange by saturation power; $R_{1\rho}$, longitudinal relaxation in the rotating frame; R_{eff} , effective relaxation rate in the rotating frame, $R_{1\rho}$ of water; R_{ex} , exchange-dependent relaxation rate; ROI, region of interest; SAR, specific absorption rate; t_{sat} , duration of pre-saturation; Z_{lab} , Z-value at the labeled frequency; Z_{ref} , Z-value at the reference frequency.

The problem of separating exchange rate and relative concentration was first reported to be solvable by the dispersion of a CEST effect with the RF saturation amplitude (B_1) (QUESP (11), multiple B_1 fit (14,21,22)). Dixon *et al.* (25) even showed that this dispersion can be transformed into a linear function of $1/B_1^2$, the so-called Ω -plot, forming a simple quantification method by linear regression. However, this method was limited to PARACEST agents due to its requirement for large chemical shifts to avoid issue (ii) outlined above: direct saturation of water with the concomitant spillover effect.

The spillover effect has recently been shown to be efficiently corrected by the inverse metric (10). Sun *et al.* (13,26) even showed that this inverse metric is actually compatible with the Ω -plot formalism and therefore application of this technique is possible in the case of small chemical shift ranges from endogenous CEST agents. However, this spillover-corrected Ω -plot method can only be utilized for the quantification of experiments using continuous wave (cw) saturation, which is not feasible on human-accessible scanners.

The goal of this study was to extend the spillover-corrected Ω -plot method for the case of pre-saturation using trains of Gaussian-shaped RF pulses. The calculations were performed analytically and are based on the Bloch–McConnell (BM) equations. This yields a method that is applicable to data acquired on whole-body scanners within the SAR limits and, moreover, is able to separately quantitatively determine relative concentrations and exchange rates.

In contrast to other approaches integrating the B_1 field strength of time-dependent pulses (cw power equivalent (24)), the presented approach is based on the R_{1p} model for CEST (27) and the integration of the longitudinal relaxation rate in the rotating frame $R_{1p}(B_1(t))$ as a function of the pulse shape. This approach allows the calculation of form factors for the modified CEST signal as well as the modified B_1 dispersion of the CEST effects generated by a series of Gaussian-shaped saturation pulses. These form factors translate directly to the Ω -plot equations for prediction of exchange rate k_{BA} and relative proton concentration f_B .

Thus we propose not only an analytic description of Z-spectra in the case of pulsed CEST, but also the application of the theory by proposing a quantitative CEST-MRI method using Ω -plots.

THEORY

Two-pool model and Ω -plot for cw saturation

We assume a system consisting of an abundant water proton pool (pool A) and a rare proton pool (pool B), which are in chemical exchange. Due to different chemical shifts, the magnetization of pool B can be reduced by selective irradiation with RF pulses at a specific frequency offset $\Delta\omega$ from water. After chemical exchange, the reduced z-magnetization $M(\Delta\omega)$ of the water protons can be measured. The normalized water signal over the irradiation range leads to the so called Z-spectrum ($Z(\Delta\omega) = M(\Delta\omega)/M_0$). The dynamic of the magnetization of this coupled system under RF irradiation is described by the BM equations (28). Solving these leads to the following analytical expression for the Z-spectrum under cw irradiation (10):

$$Z(\Delta\omega) = \cos^2\theta \frac{R_{1A}}{R_{1p}(\Delta\omega)} \quad [1]$$

where R_{1A} is the longitudinal relaxation rate of water. The longitudinal relaxation rate in the rotating frame R_{1p} is given by

$$R_{1p}(\Delta\omega) = R_{\text{eff}}(\Delta\omega) + R_{\text{ex}}(\Delta\omega) \quad [2]$$

where R_{eff} describes the relaxation due to direct water saturation,

$$\begin{aligned} R_{\text{eff}}(\Delta\omega) &= R_{1A}\cos^2\theta + R_{2A}\sin^2\theta \\ &= R_{1A} + (R_{2A} - R_{1A}) \frac{\omega_1^2}{\omega_1^2 + \Delta\omega^2} \end{aligned} \quad [3]$$

and where $\omega_1 = \gamma B_1$ is the amplitude of the saturating field, γ is the gyromagnetic ratio for protons and $\theta = \arctan(\omega_1/\Delta\omega)$ describes the angle between the effective field B_{eff} and the z-axis. The exchange-dependent relaxation R_{ex} induces the CEST effect and can be approximated as on resonance for the CEST pool by (10)

$$R_{\text{ex}} = f_B k_{BA} \frac{\omega_1^2}{\omega_1^2 + k_{BA}(k_{BA} + R_{2B})} \quad [4]$$

where R_{2B} is the transversal relaxation rate of pool B. Assuming a reference point (Z_{ref}) where R_{ex} is zero allows isolation of R_{ex} employing the relaxation-compensated metric *apparent exchange-dependent relaxation* (AREX). Using Equations [1] and [2], the inverse difference of the label and reference scans and multiplication by R_{1A} leads to the definition of AREX (10):

$$\text{AREX} =: \left(\frac{1}{Z_{\text{lab}}} - \frac{1}{Z_{\text{ref}}} \right) R_{1A} = \frac{R_{\text{ex}}}{\cos^2\theta R_{1A}} \cdot R_{1A} \stackrel{\cos^2\theta \approx 1}{\approx} R_{\text{ex}} \quad [5]$$

as $\cos^2\theta \approx 1$ in the case of $\Delta\omega \gtrsim \omega_1$. By isolating R_{ex} , investigation of the Ω -plot method applied to the AREX signal is enabled. Applying the analytical formula for R_{ex} (Equation [4]) leads to the definition of the relaxation-compensated Ω -plot:

$$\frac{1}{\text{AREX}} = \frac{k_{BA} + R_{2B}}{f_B} \frac{1}{\omega_1^2} + \frac{1}{f_B k_{BA}}. \quad [6]$$

This is a linear equation of the form

$$\frac{1}{\text{AREX}} \left(\frac{1}{\omega_1^2} \right) = m \frac{1}{\omega_1^2} + n. \quad [7]$$

Determination of the slope m and y-intersection n enables quantification of f_B and k_{BA} using the following equations (in accordance with calculations of Wu *et al.* (13)):

$$f_B = \frac{1}{n \left(-\frac{R_{2B}}{2} + \sqrt{\frac{R_{2B}^2}{4} + \frac{m}{n}} \right)} \quad [8]$$

$$k_{BA} = -\frac{R_{2B}}{2} + \sqrt{\frac{R_{2B}^2}{4} + \frac{m}{n}}. \quad [9]$$

Analytical solution and Ω -plot for pulsed saturation

To extend the Ω -plot method for the case of pulsed CEST, we used the solution for pulsed spin-lock by Roeloffs *et al.* (29). Under the assumption of R_{1p} decay during the saturation pulse of duration t_p for each individual pulse and R_{1A} recovery during the interpulse delay t_d , the steady-state Z-spectrum in the pulsed

CEST experiment is given by (10)

$$Z_{\text{pulsed}}^{\text{SS}}(\Delta\omega) = \frac{(1 - e^{-R_{1A}t_d}) - \frac{\cos(\theta)R_{1A}}{\bar{R}_{1p}(\Delta\omega)}(1 - e^{\bar{R}_{1p}(\Delta\omega)t_p})}{e^{\bar{R}_{1p}(\Delta\omega)t_p} - e^{-R_{1A}t_d}} \quad [10]$$

where $\bar{R}_{1p}(\Delta\omega)$ is the average longitudinal relaxation rate in the rotating frame. This corresponds to the solution of Santyr *et al.* (30) and Roeloffs *et al.* (29), and is valid if $k_{BA} \gg R_{1A}$ (10). Assuming small arguments for the exponential functions ($\exp(x) \approx 1 + x$), a small angle θ ($\cos(\theta) \approx 1$), and introducing the duty cycle $DC = t_p/(t_p + t_d)$, one can derive a function for the steady state as (Appendix A1)

$$Z_{\text{pulsed}}^{\text{SS}}(\Delta\omega) \approx \frac{R_{1A}}{R_{1p}(\Delta\omega)DC + R_{1A}(1 - DC)}. \quad [11]$$

Equations [8] and [9] are only valid for saturation with constant amplitude. For shaped pulses, a time-dependent $\omega_1(t)$ has to be taken into account:

$$R_{1,p}(\omega_1(t)) = R_{\text{eff}}(\omega_1(t)) + R_{\text{ex}}(\omega_1(t)). \quad [12]$$

Previous approaches (10,29,31) can be understood by implicitly using $\bar{R}_{1p} = R_{1p}(\bar{\omega}_1) = R_{1p}\left(\frac{1}{t_p} \int_0^{t_p} \omega_1(t) dt\right)$. Our approach to calculate the average \bar{R}_{1p} in the pulsed case is the integration of R_{1p} as a function of the pulse duration:

$$\begin{aligned} \bar{R}_{1p} &= \frac{1}{t_p} \int_0^{t_p} R_{1p}(t) dt \\ &= R_{1A} + \frac{1}{t_p} \int_0^{t_p} (R_{2A} - R_{1A}) \frac{\omega_1^2(t)}{\omega_1^2(t) + \Delta\omega^2} dt \\ &\quad + \frac{1}{t_p} \int_0^{t_p} f_B k_{BA} \frac{\omega_1^2(t)}{\omega_1^2(t) + k_{BA}(k_{BA} + R_{2B})} dt \end{aligned} \quad [13]$$

where R_{2A} is the transversal relaxation rate of pool A. For Gaussian-shaped pulses it can be shown (Appendix A2) that the characteristic relaxation rate R_{1p} can be described on average by a time-independent ω_1 and the form factors c_1 and c_2 with

$$\begin{aligned} R_{1p}^{\text{shaped-pulses}} &\approx R_{1A} + (R_{2A} - R_{1A}) \cdot c_1 \cdot \frac{\omega_1^2}{\omega_1^2 + \Delta\omega^2 \cdot c_2^2} \\ &\quad + f_B k_{BA} \cdot c_1 \cdot \frac{\omega_1^2}{\omega_1^2 + k_{BA}(k_{BA} + R_{2B}) \cdot c_2^2} \end{aligned} \quad [14]$$

where c_1 and c_2 depend only on the width σ and length t_p of one Gaussian-shaped pulse. They are defined as

$$c_1 = \frac{\sigma\sqrt{2\pi}}{t_p} \quad [15]$$

$$c_2 = c_1 \cdot \sqrt{\frac{2}{\pi}} = \frac{\sigma\sqrt{2\pi}}{t_p} \cdot \sqrt{\frac{2}{\pi}} \quad [16]$$

Thus, AREX in the case of pulsed pre-saturation is modified compared with an experiment using cw irradiation, whereby

$$\text{AREX}_{\text{cw}} = f_B k_{BA} \frac{\omega_1^2}{\omega_1^2 + k_{BA}(k_{BA} + R_{2B})} \quad [17]$$

and AREX in an experiment using pulsed irradiation translates to

$$\text{AREX}_{\text{pulsed}} = DC \cdot f_B k_{BA} \cdot c_1 \cdot \frac{\omega_1^2}{\omega_1^2 + k_{BA}(k_{BA} + R_{2B}) \cdot c_2^2} \quad [18]$$

This means that the principal behavior of pulsed CEST is the same as that of cw CEST, though the magnitude of the pulsed CEST effect is lowered by a factor of $DC \cdot c_1$, thus c_1 can be interpreted as an 'intra-pulse duty cycle'. In addition, the B_1 dispersion of AREX is altered due to the pulse shape to an effective value $\frac{\omega_1}{c_2}$. For example, the rough estimation of $\omega_1 \sim k_{BA}$ for 50% labeling efficiency in cw CEST effects (2) is changed to $\omega_1 \sim k_{BA} c_2$. Thus, an optimal B_1 found for cw irradiation can be translated into an optimal B_1 for a pulsed CEST experiment by a reduction of a factor $c_2 = c_1 \cdot \sqrt{2}$. For the Gaussian-shaped pulses employed in this work, the form factors are $c_1 = 0.5623$ and $c_2 = 0.6687$. In the case of an experiment with spin-lock pulses, the form factors are $c_1 = c_2 = 1$.

We need to point out that, according to Equation [A18], B_1 values in the pulsed case refer to the average amplitude of the pulse. This corresponds to the flip angle of the pulse divided by t_p and is not the same as the cw amplitude equivalent ($B_{1\text{cwae}}$) or cw power equivalent ($B_{1\text{cwpe}}$) as given in Reference 24. The relation between B_1 here and $B_{1\text{cwae}}$ is $B_1 = B_{1\text{cwae}} \cdot DC$.

Ω -plot for shaped pulses

Using Equation [18] and similarly repeating the calculations as for the determination of Equations [8] and [9] yields the following novel Ω -plot formulae to determine f_B and k_{BA} for pre-saturation with a Gaussian-shaped pulse train:

$$f_B^{\text{shaped-pulses}} = \frac{1}{c_1 \cdot DC \cdot n \cdot \left(-\frac{R_{2B}}{2} + \sqrt{\frac{R_{2B}^2}{4} + \frac{m}{n \cdot c_2^2}}\right)} \quad [19]$$

$$k_{BA}^{\text{shaped-pulses}} = -\frac{R_{2B}}{2} + \sqrt{\frac{R_{2B}^2}{4} + \frac{m}{n \cdot c_2^2}} \quad [20]$$

MATERIALS AND METHODS

Phantoms

For MR measurements at $B_0 = 7\text{ T}$, three sets of phantoms were employed, each containing seven 30 mL tubes (Table 1). Phantom 1 consisted of creatine monohydrate (Sigma-Aldrich, Steinheim, Germany) of varying concentrations c_{Cr} , while for Phantom 2 the pH was varied and, finally, for Phantom 3 the longitudinal relaxation times of water T_{1A} and transversal relaxation times of water T_{2A} were varied, induced by gadolinium (Gd-DTPA; Magnevist, Bayer Schering Pharma, Berlin, Germany) doping and changing the agar concentration, respectively. The longitudinal relaxation times T_{1A} for Phantoms 1 and 2 as well as for Tubes 1–4 in Phantom 3 were measured to be $4.31 \pm 0.13\text{ s}$. The T_{1A} values for Tubes 5–7 in Phantom 3 were $0.95 \pm 0.05\text{ s}$ (Tube 5), $0.69 \pm 0.04\text{ s}$ (Tube 6), and $0.45 \pm 0.09\text{ s}$ (Tube 7). The transversal relaxation times T_{2A} were not measured; however, for the chosen agar concentrations they should be in the range of 1.6 s (0% agar) and 0.13 s (1% agar) according to Zaiss *et al.* (10). The resonance of the guanidinium group ($-\text{NH}_2$)₂ of creatine is located at $\sim 1.9\text{ ppm}$ in the Z-spectrum (31). The temperature of the phantoms was stabilized at 37°C using an

Table 1. Composition of the three phantoms. Phantom 1 contains varying creatine concentrations c_{Cr} , Phantom 2 contains solutions of varying pH, while Phantom 3 contains varying gadolinium (Gd-DTPA; Magnevist, Bayer Schering Pharma, Berlin, Germany) and/or agar concentrations

		Tube	1	2	3	4	5	6	7
Phantom 1	pH 7.15	c_{Cr} [mM]	10	20	35	50	75	100	125
Phantom 2	$c_{Cr} = 50$ mM	pH	6.32	6.54	6.74	6.94	7.15	7.40	7.60
Phantom 3	pH 7.15, $c_{Cr} = 50$ mM	Gd-DTPA [μ M]	0	0	0	0	125	250	500
		Agar [%]	0.5	0.5	1	2	0.5	0.5	0.5

MR-compatible thermos flask containing 1.8 L of water. Solutions were buffered using phosphate-buffered saline with 1/15 M sodium potassium phosphate.

For MR measurements at $B_0 = 14.1$ T, a model solution of volume 1 mL was prepared in the same manner, containing $c_{Cr} = 50$ mM at pH 7.12. The temperature of the sample was set to 37 °C using the internal heating and cooling device of the spectrometer.

BM simulations

The simulation of the BM equations was realized by an in-house written MATLAB script (MathWorks, Natick, MA, USA) extended for shaped pulses by depiction of the pulse train as described in Reference 32. The following parameters, if not stated otherwise, were chosen for the simulations at a static magnetic field strength $B_0 = 7$ T. Water (phosphate-buffered saline solution): $T_{1A} = 4.2$ s, transversal relaxation time of pool A $T_{2A} = 1.2$ s and $\Delta\omega_A = 0$ ppm. A creatine-like pool was assumed with $T_{1B} = T_{1A}$, $T_{2B} = 1/66.66$ s (8), $f_B = 2.00\%$, $k_{BA} = 945$ s⁻¹ and $\Delta\omega_B = 1.9$ ppm (31).

CEST spectroscopy at 14.1 T

The comparison of cw and pulsed CEST experiments was performed on a 14.1 T narrow bore spectrometer (Bruker, Karlsruhe-Rheinstetten, Germany) equipped with a 5 mm probe. Z-spectra (number of excitations = 1) were obtained using various saturation RF amplitudes ($B_1 = 0.5, 0.75, 1.25, 1.75$, and 2.5 μ T) and a saturation duration t_{sat} of 14.1 s. B_1 values in the pulsed case refer to the average amplitude of the pulse according to Equation [A18].

In the case of cw CEST a rectangular pulse, and in the case of pulsed CEST 71 Gaussian-shaped pulses of duration $t_p = 0.1$ s and DC = 50%, were used for pre-saturation. The width-to-pulse duration ratio $\sigma/t_p = 1/4.458$ for the Gaussian-shaped pulses leads to the form factors $c_1 = 0.5623$ and $c_2 = 0.6687$. Integration of the water resonance over the range ± 0.7 ppm yielded the signal $M(\Delta\omega)$. Z-spectra were sampled at 81 frequency offsets in uneven steps between $\Delta\omega = \pm 7.0$ ppm relative to the water resonance ($\Delta\omega = 0$ ppm). Before repetition of the pulse sequence, a waiting interval of 1 s was implemented. For normalization, a fully relaxed signal (M_0) without saturation was acquired. Measurement of T_1 (number of excitations = 1) was by means of a saturation-recovery pulse sequence using a cw, rectangular, low-power RF pulse of length 15 s to saturate the water signal. The integrated water resonances in the range of ± 0.7 ppm were fitted for 25 contrasts at different recovery times T_1 between 10 ms and 20 s to determine the T_{1A} of water.

CEST imaging at 7 T and Ω -plots

The CEST experiments on the phantoms were conducted with a 7 T whole-body MR tomograph (MAGNETOM 7 T; Siemens Healthcare,

Erlangen, Germany) using a 28-channel Tx/Rx ¹H knee coil. The images were acquired by a centric-reordered two-dimensional gradient echo (GRE) sequence: number of excitations = 1, field of view (FoV) 180×180 mm², matrix 128×128 , slice thickness 5 mm, flip angle 10°, repetition time $T_R = 6.9$ ms, echo time $T_E = 3.36$ ms. Saturation was achieved using a pulse train of $t_{sat} = 10$ s consisting of 50 Gaussian-shaped pulses of duration $t_p = 0.1$ s and DC = 50%. Six different B_1 amplitudes were chosen: 1.17, 1.36, 1.56, 1.75, 1.94, and 2.33 μ T. Forty-three evenly distributed frequency offsets were measured between ± 4 ppm. Additionally, an unsaturated image M_0 was acquired at +300 ppm. The ratio σ/t_p of the Gaussian-shaped pulses is the same as for the pulses used on the 14.1 T spectrometer, leading to the same form factors. T_1 mapping was achieved by fitting T_1 -weighted images of a saturation-recovery GRE sequence (number of excitations = 1, FoV 180×180 mm², matrix 128×128 , slice thickness 5 mm, flip angle 8°, $T_R = 8000$ ms, $T_E = 1.36$ ms) with 22 recovery times between 0.25 and 7.5 s. Z-spectra were linearly interpolated and B_0 -corrected employing a WASSR map (33) and B_1 -corrected using the evaluation method of Windschuh *et al.* (34). Ω -plots were evaluated pixel-wise using a linear regression method based on the Levenberg–Marquardt algorithm (35).

RESULTS

Analytical solution for the simulation of Gaussian-shaped pulses and the Ω -plot

For a first attempt, the full BM simulation for Gaussian-shaped pulses ($n = 60$, $t_p = 0.1$ s, DC = 50%) was compared with the analytical model described by Equation [10]. Simulation of the system over a broad range of different B_1 , f_B , and k_{BA} values (Fig. 1(A)–(C)) revealed that the analytical model, Equation [12], agrees with the BM simulations. The Z-spectra deviate from prediction only close to the water resonance. It is worth noting that the analytical simulation for Gaussian-shaped pulses was approximately 5500 times faster than the numerical simulation (both simulations performed with MATLAB on a 3.2 GHz dual core CPU). Additionally, a saturation transfer experiment with spin-lock pulses was simulated using the analytical solution by Roeloffs *et al.* (29) (Fig. 1(A)). As expected, the analytical spin-lock solution differs from the simulations with Gaussian-shaped pulses.

To demonstrate the functionality of our extended Ω -plot method, we calculated the inverted AREX values at 1.9 ppm ($Z_{lab} = Z(1.9$ ppm), $Z_{ref} = Z(-1.9$ ppm)) for the numerical simulation of the Gaussian-shaped pulse shown in Fig. 1(A) as a function of $1/\omega_1^2$ (Fig. 1(D)). For this simulation, the tuple (k_{BA} [s⁻¹] | f_B [%]) = (945 | 2.00) was used for the exchange rate and concentration. Indeed, the pulsed data also show a clear linear behavior (Fig. 1(D), circles). Fitting the data points with a linear function (dashed line) enables application of Equations [19] and [20], yielding (k_{BA} [s⁻¹] | f_B [%]) = (906 \pm 57 | 2.08 \pm 0.04). Without a

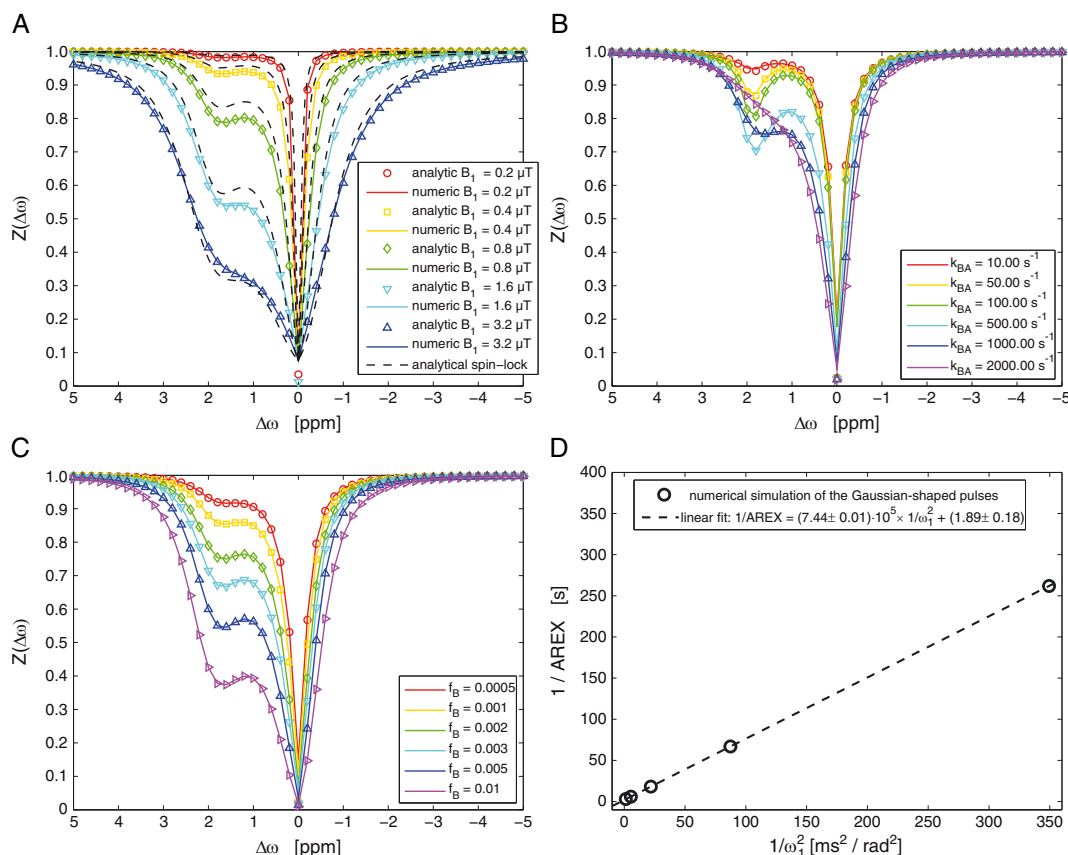


Figure 1. (A)–(C) Analytical (lines) and numerical (marker) simulation of Z-spectra using saturation by trains of Gaussian-shaped RF pulses ($n = 60$, $t_p = 0.1$ s, DC = 50%, same σ/t_p ratio as in the experiments at $B_0 = 14.1$ T) with various B_1 (A), k_{BA} (B), and f_B (C) values. The creatine guanidinium proton pool, which resonates at 1.9 ppm, was simulated using $k_{BA} = 945$ s $^{-1}$ and $f_B = 2.00\%$. The B_1 -dependence of a pulsed spin-lock experiment (the analytical solution is from Reference 29) is also shown in (A). (D) The Ω -plot resulting from the numerical simulation displays the expected linearity. AREX was determined using $Z_{lab} = Z(1.9$ ppm), $Z_{ref} = Z(-1.9$ ppm) and $T_{1A} = 4.2$ s.

correction for Gaussian-shaped pulses (i.e. Equations [19] and [20] with $c_1 = c_2 = 1$, DC = 50%), the Ω -plot method generates a less accurate estimation: $(k_{BA}$ [s $^{-1}$] $|f_B$ [%]) = $(595 \pm 57|1.78 \pm 0.04)$. Using the cw solution directly (Equations [8] and [9]) yields $(k_{BA}$ [s $^{-1}$] $|f_B$ [%]) = $(595 \pm 57|0.89 \pm 0.04)$.

Comparison of pulsed and cw solutions for Ω -plots

To experimentally compare a pulsed with a cw CEST quantification, an MR spectrometer with cw irradiation capability was used and both cw and pulsed pre-saturation were applied (Fig. 2(A)). The longitudinal relaxation rate of the model solution was determined to be $T_{1A} = 3.62 \pm 0.24$ s. Ω -plot quantification (Fig. 2(B), dashed line) of the cw CEST experiment (circles) using Equations [8] and [9] yielded $(k_{BA}$ [s $^{-1}$] $|f_B$ [%]) $_{cw} = (911 \pm 123|1.72 \pm 0.34)$. Evaluation of the pulsed-CEST experiment (Fig. 2(B), squares) with the derived Gaussian Ω -plot method (dotted line) using Equations [19] and [20] yielded $(k_{BA}$ [s $^{-1}$] $|f_B$ [%]) $_{Gaussian} = (838 \pm 326|1.88 \pm 0.16)$, which agrees within the errors with the value using cw pre-saturation. Without the correction for Gaussian-shaped pulses (i.e. Equations [19] and [20] with $c_1 = c_2 = 1$, DC = 50%), the Ω -plot method generates a more biased estimation: $(k_{BA}$ [s $^{-1}$] $|f_B$ [%]) = $(550 \pm 218|1.62 \pm 0.13)$. Using the cw solution directly (Equations [8] and [9]) yields $(k_{BA}$ [s $^{-1}$] $|f_B$ [%]) = $(550 \pm 218|0.81 \pm 0.13)$.

Accuracy of k_{BA} and f_B in simulations

To further evaluate the extended Ω -plot method proposed in this study, we applied it to data from a pulsed two-pool BM simulation (Fig. 3). This allows testing of the influences of a broad range of values for the CEST parameters f_B and k_{BA} (Fig. 3(A), (C)), as well as the water pool relaxation parameters T_{1A} and T_{2A} (Fig. 3 (B), (D)). The comparison of the values obtained for f_B and k_{BA} with the theoretical values from the simulation revealed that the proposed Ω -plot method works with less than 15% deviation for $0.07\% < f_B < 1\%$, 150 s $^{-1} < k_{BA} < 2000$ s $^{-1}$, 0.5 s $< T_{1A} < 4.2$ s, 0.05 s $< T_{2A} < 1$ s; in extreme cases larger deviations are observed, marked by blue or red color in Fig. 3. As expected, prediction using this method fails for very slow exchange rates (< 50 s $^{-1}$) (10). Still, there are minor influences of water relaxation times, which might originate from violations of the steady-state condition.

Ω -plots of phantom measurements

Region-of-interest (ROI) averaged AREX values were calculated for phantoms with varying creatine concentrations, varying pH values, and varying water relaxation values. For all phantoms, the Ω -plots, which are given by $1/\text{AREX}$, are linear functions of $1/\omega_1^2$ (Fig. 4). The fact that this linearity is also present in the case of pulsed pre-saturation already indicates that the principal formula for R_{ex} – especially the B_1 dispersion – must have the same

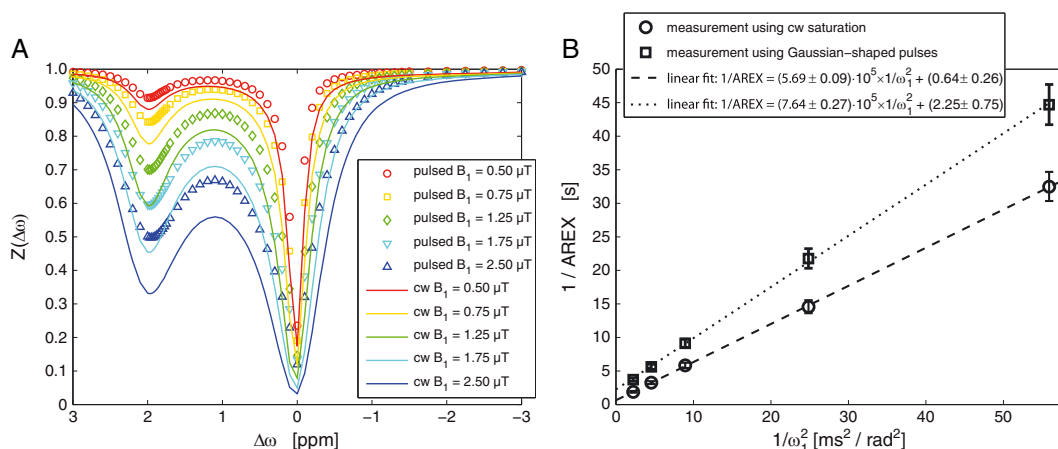


Figure 2. (A) Experimental Z-spectra for cw saturation (lines) and saturation using Gaussian-shaped pulses (marker) with various B_1 values obtained from model solution measurements ($c_{\text{Cr}} = 50$ mM, pH 7.12, $T = 37^\circ\text{C}$) at $B_0 = 14.1$ T. The saturation time was $t_{\text{sat}} = 14.1$ s for cw, whereas for the pulsed saturation 71 Gaussian-shaped pulses with $t_p = 0.1$ s and DC = 50% were used. For the same saturation amplitudes, the cw measurement shows a larger CEST effect compared with the pulsed pre-saturation. (B) The corresponding Ω -plots display the expected linearity. The calculated form factors for the Gaussian-shaped pulses are $c_1 = \sigma/t_p\sqrt{2\pi} = 0.5623$ and $c_2 = c_1\sqrt{2} = 0.6687$.

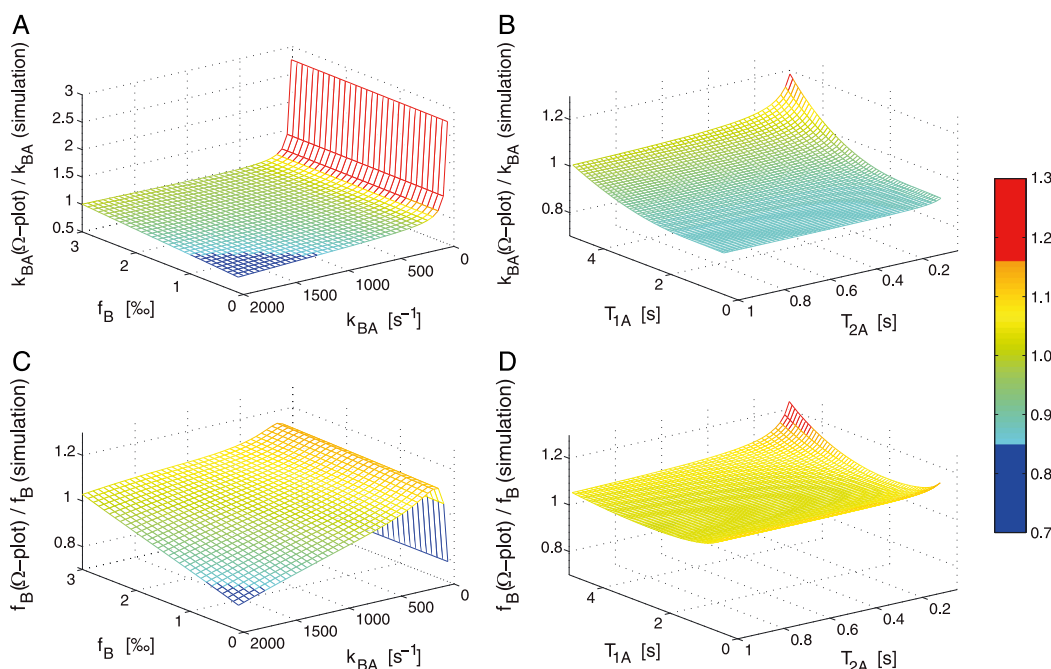


Figure 3. The accuracy of the CEST analysis using the extended Ω -plot method for simulations is shown. The normalized exchange rate is displayed as a function of exchange rate k_{BA} and relative proton concentration f_{B} (A) and as a function of relaxation times T_{1A} and T_{2A} of the water pool (B). The normalized labile proton concentration is also shown as a function of exchange rate k_{BA} and labile proton concentration f_{B} (C) and as a function of relaxation times T_{1A} and T_{2A} of the water pool (D). The color bar applies to all graphs. Saturation was always carried out using 60 Gaussian-shaped pulses ($t_p = 0.1$ s, DC = 50%, same σ/t_p ratio as in the experiments at $B_0 = 14.1$ T).

form for pulsed and cw pre-saturation. This experimental finding encouraged the integration approach given in Appendix A2, which explains the observed behavior as expressed in Equations [17] and [18]. Equations [19] and [20] can thus be used for evaluation of pixel-wise calculated Ω -plots. Applied to phantom imaging data, we were able to reconstruct quantitative maps for k_{BA} and f_{B} within minutes (Fig. 5). For Phantom 1 (Fig. 5(A), (B)), with varying creatine concentrations, the k_{BA} map is homogeneous across the tubes whereas the f_{B} map scales correctly with c_{Cr} . For Phantom 2 (Fig. 5(C), (D)), with varying pH, the k_{BA} map correlates with pH whereas the f_{B} map remains homogeneous

and stable between the tubes. The control for water relaxation influences (Fig. 5(E), (F)) shows only very small differences between tubes in both the k_{BA} and f_{B} maps.

Thus, the qualitative behavior of our Z-spectrum model and extended Ω -plot method has been verified. To also check the quantitative values of the exchange rate k_{BA} and the concentration f_{B} in each tube, an ROI evaluation was performed (Fig. 6). The evaluated creatine exchange rate k_{BA} (Fig. 6(A) and (E), blue squares) is very close to our 'ground truth', the value $911 \pm 123 \text{ s}^{-1}$ (dotted line) determined here in the cw experiment at 14.1 T (Fig. 2), as well as to the published (36) value of $950 \pm 100 \text{ s}^{-1}$ (Fig. 6(A),

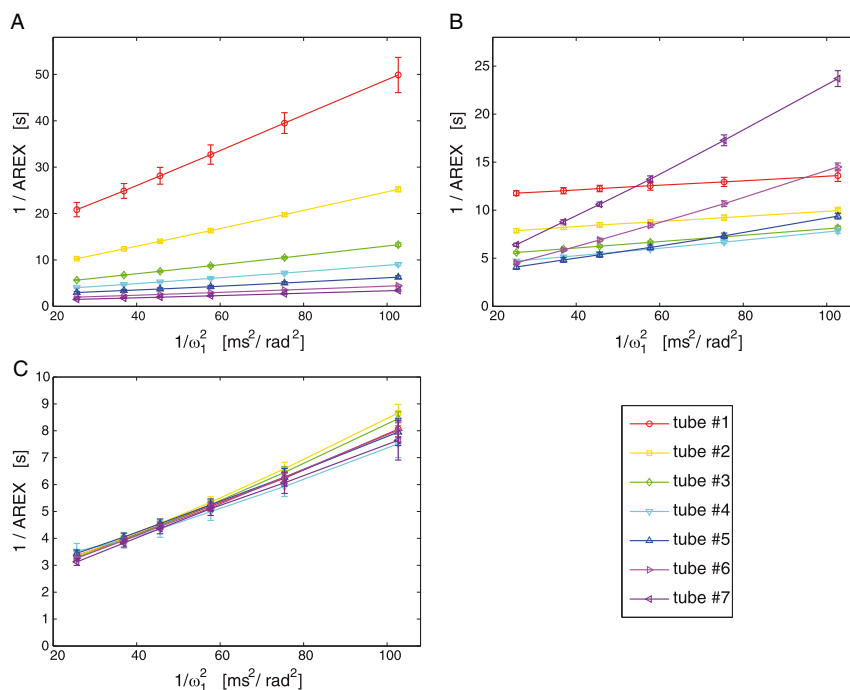


Figure 4. Ω -plots determined from ROI analysis of the three phantoms (Table 1). To evaluate the phantoms, all pixels within each tube were selected and averaged. The linearity is given for the entire range of the creatine concentrations (A), pH values (B), and water relaxation parameters (C). Whereas the Ω -plots in Phantom 1 (A) and Phantom 2 (B) show a different behavior for each tube, the different relaxation parameters in Phantom 3 (C) yield the same Ω -plots within the error limits. The legend refers to the numbering used in Table 1.

dashed line). The concentration f_B scales linearly with the concentration of creatine (Fig. 6(B)), and the magnitude obtained by the new evaluation improves the estimation compared with the theoretical values for f_B assuming four exchanging protons of the creatine guanidinium group (10,31) across the range of creatine concentrations c_{Cr} (Fig. 6(B), (D) and (F), solid line). The exchange rate k_{BA} (Fig. 6(C)) shows exponential behavior as a function of pH, as expected for a base-catalyzed proton exchange (37).

In summary, the extended Ω -plot method for pulsed pre-saturation based on the AREX evaluation (Equation [18]) is able to accurately determine the concentration of a CEST agent as well as the exchange rate as a function of pH.

DISCUSSION

In this paper we propose a solution to the lingering problem of quantification of CEST data obtained using pulsed pre-saturation, as it would be from a clinical setting. By extension of the Ω -plot method of Dixon *et al.* (25), we derived two form factors for transforming the current Z-spectrum model for saturation with a Gaussian-shaped pulse train. The whole approach is based on the assumption that the behavior of the magnetization during a Gaussian-shaped pulse train can be described by an $R_{1\rho}$ decay during the saturation pulse and an R_{1A} recovery during the interpulse delay. This had already been demonstrated for spin-lock by Santyr *et al.* (30) and Roeloffs *et al.* (29). Our extended approach of using an integrated $R_{1\rho}$ over the pulse shape also enables the quantification of f_B and k_{BA} in the case of pre-saturation by a train of Gaussian-shaped RF pulses.

Z-spectrum model

The presented model (Equation [10]) is based on several key principles and conditions. First of all, we used the longitudinal relaxation rate in the rotating frame $R_{1\rho}$, which had been proposed for spin-lock by Trott and Palmer (38) and extended for CEST experiments by Zaiss *et al.* (27). This approach requires, first, small CEST pools ($f_B < 1\%$), and, second, sufficiently long saturation times ($t_{sat} > T_{2A}$). Both of these conditions are met for typical CEST experiments for metabolites in low concentrations and saturation duration in the range of T_{1A} .

The next step for modeling the Z-spectrum was an effective depiction of the pulses and the interpulse delays, which was shown to be successful in the case of spin-lock by Roeloffs *et al.* (29). In the presented model, we neglect the exchange dynamic in the interpulse delay, which has been shown (29) to be very important in the case of slow exchange rates ($k_{BA} \approx 1/t_d$). Hence a meaningful evaluation of a Z-spectrum using Equation [10] can be anticipated when this contribution is negligible, thus leading to the third limitation, namely $k_{BA} > 1/t_d$.

A further step, namely the integration of $R_{1\rho}$ over the RF pulse, had already been successfully applied to adiabatic spin-lock pulses (39). This encouraged us to use the same approach for Gaussian-shaped pulses which are adiabatic in the off-resonance case (40). According to Zu *et al.* (40), our pulse has an adiabaticity of $\eta \geq 50.5$ ($B_1 = 3.2 \mu T$, $\Delta\omega = 1.9$ ppm), which clearly satisfies the adiabatic condition ($\eta \gg 1$). However, this condition might be violated close to the water resonance ($\Delta\omega < 0.5$ ppm), and deviations from the theory could thus occur. Furthermore, the analytical integral (Equation [A20]) is only valid in the case $\Delta\omega > \omega_1$, which therefore forms the fourth theoretical limit of the approach.

Another significant problem with short pulses are the induced rotations of the magnetization around B_{eff} , which are not modeled

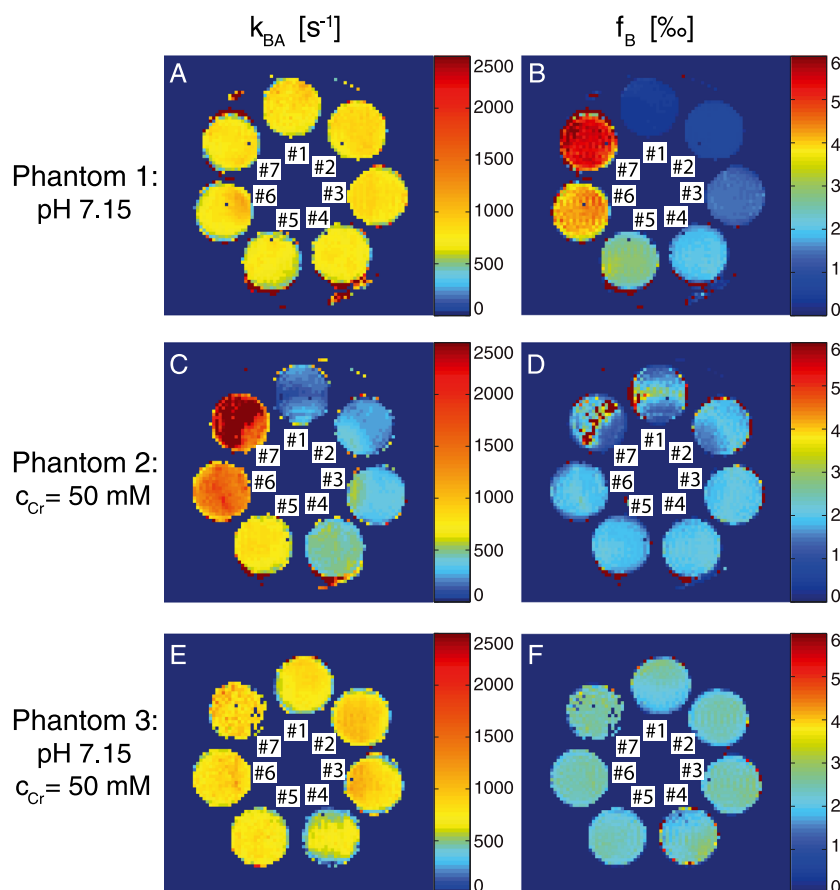


Figure 5. Maps obtained by pixel-wise fitting of the Ω -plots yield the exchange rate k_{BA} ((A), (C), and (E)) and concentration f_B ((B), (D), and (F)) for Phantoms 1–3. The exchange rates for Phantom 1 (pH 7.15, c_{Cr} = 10, 20, 35, 50, 75, 100, and 125 mM) show mostly no change (A), whereas the concentration shows a strong dependence on c_{Cr} (B). In Phantom 2 (c_{Cr} = 50 mM, pH 6.32, 6.54, 6.74, 6.94, 7.15, 7.40, 7.60), the relations are the opposite ((C), (D)). The results in Phantom 3 (pH 7.15, c_{Cr} = 50 mM, [Gd] = 0, 0, 0, 125, 250, and 500 μ M, agar = 0.5, 0.5, 1, 2, 0.5, 0.5, and 0.5%) show mostly no variations for the selected relaxation parameter ((E), (F)). For better visualization, all pixels with an asymmetry $MTR_{asym} < 0.04$ were set to 0. The artifacts in Phantom 2 (especially Tubes 1 and 7) result from an incomplete B_1 -correction ((C), (D)). The numbering in the maps refers to Table 1.

by the single eigenvalue approach (9,2741). Consequently, chemical exchange rotation transfer (CERT) (42) cannot be accurately described by the presented approach, as has been pointed out by Roeloffs *et al.* (29). However, CERT effects are only dominant for slow exchange, thus the fifth limitation is a sufficiently large exchange rate k_{BA} , i.e., the pulse dynamic should be slower than the exchange dynamic to allow for proper integration ($k_{BA} > 1/t_p$). Violation of this condition contributes to the deviations observed for small exchange rates ($k_{BA} < 50 \text{ s}^{-1}$, Fig. 3(A), (C)).

Some deviations can also be expected due to the fact that R_{1p} was integrated over one pulse from $t = -\infty$ to $t = +\infty$ (Equations [A17]–[A19]). However, a Gaussian-shaped pulse, as generated by an RF amplifier, is finite and values near the edges are modified in comparison to a Gaussian function to compensate for artifacts. Integration of these modified real-time pulses is analytically not that simple. Thus, the derived form factors c_1 and c_2 are only approximations and should vary slightly for pulses used on an MR tomograph. This approximation worsens as σ/t_p increases. In this case, the exact integration can be performed numerically, leading to exact form factors c_1 and c_2 for any given pulse shape. This procedure applied to our Gaussian pulses leads, in contrast to the analytical derived $c_1 = 0.5623$ and $c_2 = 0.6687$, to $c_1 = 0.5672$ and $c_2 = 0.6171$, which further improved the goodness of the estimation of k_{BA} and f_B by the AREX-based Ω -plot method (Supplementary Fig. S1).

In summary, the proposed Z-spectrum model is valid if the following conditions are met: (i) $f_B < 1\%$, (ii) $t_{sat} > T_{2A}$, (iii) $k_{BA} > 1/t_d$, (iv) $\Delta\omega \gtrsim \omega_1$, (v) $k_{BA} > 1/t_p$, and (vi) $\sigma/t_p \leq 0.5$. Consequently, the RF pre-saturation pulses must contain at least 2σ of the real Gaussian pulse and its duration, and also the interpulse delay must be longer than $1/k_{BA}$. These restrictions can be fulfilled on clinical systems for typical CEST systems in the intermediate exchange regime. Interestingly, the analytical Z-spectrum model (Equation [10]) also matches well for offsets close to 0 ppm (Fig. 1).

AREX-based Ω -plots

Since AREX represents isolated saturation transfer signals corrected for water relaxation properties, the presented Ω -plot transformation does not depend on the relaxation parameters T_{1A} and T_{2A} (Fig. 5(E), (F)). Thus, the approach represents the step from an unbiased AREX signal to a completely quantitative approach, allowing the independent determination of the relative concentration and exchange rate. A similar approach for cw saturation has been presented by Sun *et al.* (13,26).

The linearity of the Ω -plots, as expressed in Equation [7] and Appendix A2, is clear. However, this modeling was based on two further assumptions. First, small exponents in the

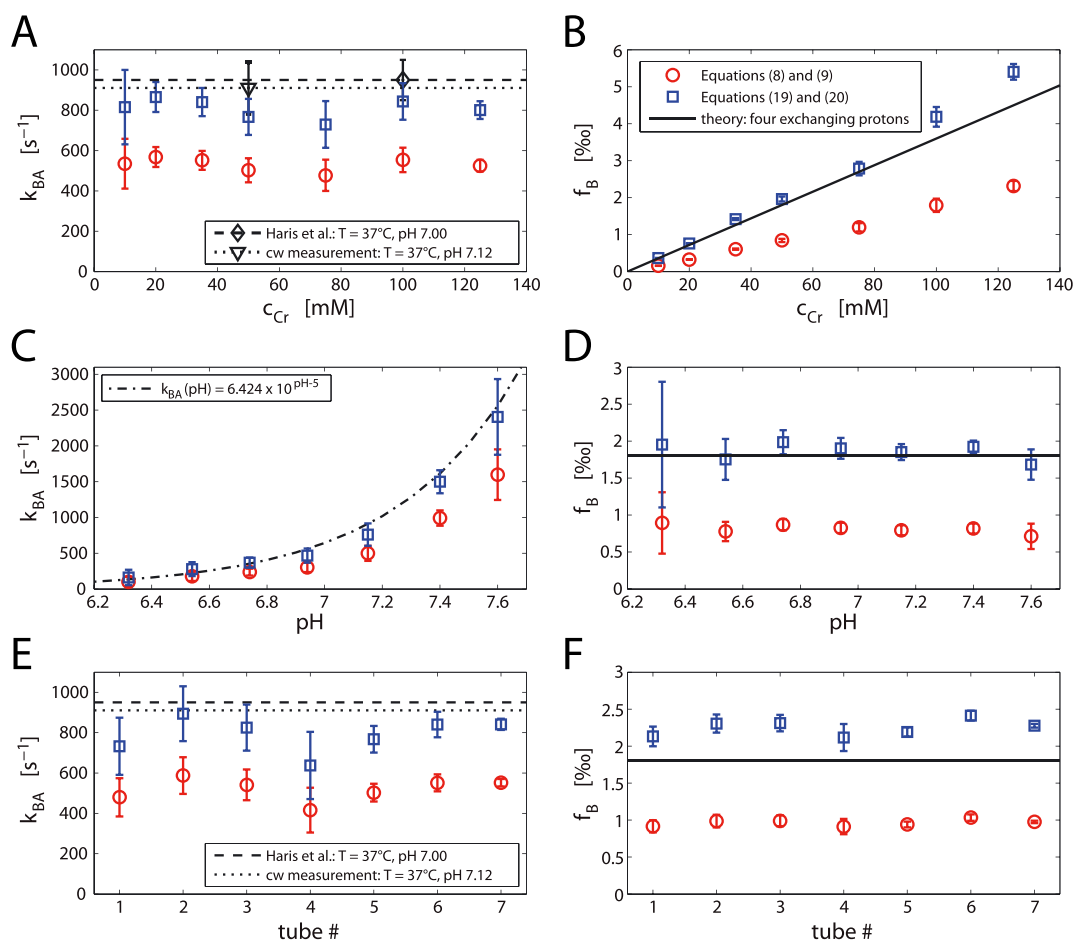


Figure 6. ROI analyses of the three phantoms for exchange rates k_{BA} (A), (C), and (E) and concentrations f_B (B), (D), and (F) are shown. To evaluate the phantoms, all pixels within each tube were selected and averaged. The saturation was always carried out with 50 Gaussian-shaped pulses with $t_p = 0.1$ s and DC = 50%, resulting in a total saturation time $t_{sat} = 10$ s. The results based on the extended Ω -plot method (Equations [19] and [20], blue squares) are shown as well as the results based on the Ω -plot method for cw pre-saturation (Equations [8] and [9], red circles). For comparison, the values $k_{BA} = 950 \pm 100 \text{ s}^{-1}$ (pH 7.00, $c_{Cr} = 100 \text{ mM}$) of Haris *et al.* (36) (diamond, dashed line) and $k_{BA} = 911 \pm 123 \text{ s}^{-1}$ (pH 7.12, $c_{Cr} = 50 \text{ mM}$) from our spectrometer cw measurement (Fig. 2, triangle, dotted line) are displayed in (A) and (E). The dependence of k_{BA} on pH correlates well with the calibrated function $k_{BA}(\text{pH}, T)$ of Goerke *et al.* (31), setting the temperature for exchange rate prediction to 31.5°C (dot-dashed line). The assumption of four exchanging protons for the creatine guanidinium group (10,31) leads to a theoretical value for f_B (solid line) that is in good agreement with our extended Ω -plot method, as shown in (B), (D), and (F).

exponential functions of Equation [10] were approximated by $\exp(x) \approx 1 + x$ to yield the simplified Equation [11]. This approximation requires $R_{1p}t_p$ and $R_{1A}t_d$ to be small ($\ll 1$). If $R_{1p} \approx 2R_{1A}$ and $t_p = t_d = 0.1$ s, then the exponents are 0.1 and 0.2, leading only to a slight underestimation of approximately 2.3%. This approximation explains the deviations for small T_{2A} values present in Fig. 3(B), (D). Second, the analytical formula describing the average $\overline{R_{1p}}$ in the case of pulsed pre-saturation (Equation [A21]) only converges if $\omega_1^2 < 0.5 \cdot k_{BA}(k_{BA} + R_{2B})$ and $\omega_1^2 < 0.5 \cdot \Delta\omega^2$. Again, this limits the proposed method to intermediate or fast exchanging protons, in contrast to the original Ω -plot method (25).

Originating from the steady-state AREX evaluation, the extended Ω -plot method is only valid for the steady-state condition ($t_{sat} \geq 5 \cdot T_{1A}$). Consequently, deviations in the quantitative parameters are apparent in phantoms with comparatively long T_{1A} (Fig. 3(B)). Even if the steady-state condition is fulfilled, a systematic error of k_{BA} and f_B is observed in the simulations (Fig. 3), which probably results, as stated above, from the theoretical integration of the Gaussian-shaped pulses in the interval from

$t = -\infty$ to $t = +\infty$ (Equations [A17]–[A19]). Again, numerically derived form factors can alleviate this systematic deviation (see Supplementary Information).

Ω -plot for shaped pulses in phantoms at 7 T

In spite of the limitations outlined above, the quantified values are in good agreement with published results: Haris *et al.* (36) determined an exchange rate for creatine of $k_{BA} = 950 \pm 100 \text{ s}^{-1}$ at pH 7.00. The value determined by the original Ω -plot method forms our 'ground truth' here and is $k_{BA} = 911 \pm 123 \text{ s}^{-1}$ at pH 7.12 (Fig. 2). Using the cw description (Equation [9]) without the form factors applied in the case of pulsed pre-saturation and averaging over the three phantoms in Fig. 5 yields $k_{BA} = 525 \pm 43 \text{ s}^{-1}$. This is greatly improved employing the extended approach (Equation [22]), yielding $k_{BA} = 800 \pm 65 \text{ s}^{-1}$.

In previous work, the creatine exchange rates for different pH values and temperatures were determined using water-exchange spectroscopy (31), a method that is only applicable at low exchange rates. In that study, the exchange rate as a function

of pH was measured at $T = 25^\circ\text{C}$ and then extrapolated to $T = 37^\circ\text{C}$. Using the Ω -plot method enables the direct measurement of intermediate exchange rates for creatine at physiological conditions. As a result, we think that the extrapolation to higher temperatures by Goerke *et al.* (31) led to an overestimated exchange rate for $k_{\text{BA}} = 1500 \pm 150 \text{ s}^{-1}$ at 37°C and that our direct measurement of $k_{\text{BA}} \approx 911 \text{ s}^{-1}$ is more reliable. Interestingly, adjusting the calibrated function $k_{\text{BA}}(\text{pH}, T)$ of Goerke *et al.* (31) by heuristically setting the temperature for exchange rate prediction to 31.5°C again yields a very nice correlation with our measured exchange rate as a function of pH ($k_{\text{BA}}(\text{pH}, 37^\circ\text{C})$, Fig. 6(C)). This corresponds to multiplication of $k_{\text{BA}}(\text{pH})$ by a factor of $c(T)$. Thus, while the calibration of k_{BA} by Goerke *et al.* for creatine is reliable in the range used for the pH and temperature, it only provides a very rough estimation of the exchange rate upon extrapolation. This again indicates that CEST approaches are more powerful than common NMR approaches for studying exchange processes in the intermediate exchange regime.

Altogether, the proposed method yields quantitative values for k_{BA} and f_{B} that are in good agreement with results determined by quantification methods using cw pre-saturation.

It should be noted that all CEST techniques – including the presented one – are prone to inhomogeneity artifacts. Based on asymmetry analysis, our approach requires a B_0 correction. This might be omitted by sophisticated sequences (42,43) or fitting approaches (21,34,44–46) that can be combined with the presented approach. In particular, the Ω -plot method, employing the B_1 dispersion of the CEST signal, requires knowledge of the actual B_1 in each pixel, or an efficient B_1 correction (34,47).

Concerning application of the proposed method *in vivo*, the apparent semi-solid magnetization transfer (MT) pool modifying $R_{1\rho}$ and R_{1A} of water (48) also has to be considered. However, as recently demonstrated (49), semi-solid MT can be described using an $R_{1\rho}$ model. Thus we think that following the approach of (49) – using the observed longitudinal relaxation rate $R_{1\text{obs}}$ and a proper reference scan Z_{ref} , which allows one to separate the effect of the CEST pool – the presented pulsed AREX-based Ω -plot method should also be feasible in the presence of a semi-solid MT. The acquisition of such a reference scan is a common problem in the field of CEST, and many techniques have been developed to obtain Z_{ref} without using the opposite frequency. These are Lorentzian difference approaches (21,34,44–46), extrapolation of MT (50), three-point methods (9,10,51), variable flip angle methods (40,42), variable delay-time approaches (43) or transfer rate edited CEST approaches (52). In a similar manner, multi-pool systems can be handled if the various signals are spectrally separated for each Ω -plot.

CONCLUSIONS

The proposed evaluation method utilizing Ω -plots allows the simultaneous determination of the concentration f_{B} of exchanging protons and their exchange rate k_{BA} in the case of pulsed pre-saturation. Based on the AREX evaluation of Z-spectra, our method is also robust against changes in water relaxation parameters. We showed that the pulsed CEST experiment can be described analytically by integrating the longitudinal relaxation rate in the rotating frame $R_{1\rho}(\omega_1(t))$ as a function of the pulse shape. Eventually we were able to derive two form factors c_1 and c_2 adjusting the cw theory for shaped pulses. Employing these form factors allows an improved estimation of f_{B} and k_{BA}

using Ω -plots for pulsed CEST experiments. Simulations show the applicability of our method to intermediate- and fast-exchanging protons. *In vitro* experiments with creatine verified the linear dependence of f_{B} on creatine concentration c_{Cr} and the exponential dependence of k_{BA} on pH. Quantified parameters in the case of a pulsed pre-saturation are in good agreement with results from cw experiments. Altogether, this approach represents a further step towards quantitative CEST studies *in vivo*.

REFERENCES

1. Zhou J, van Zijl PCM. Chemical exchange saturation transfer imaging and spectroscopy. *Prog. Nucl. Magn. Reson. Spectrosc.* 2006; 48: 109–136. DOI: 10.1016/j.pnmrs.2006.01.001.
2. Zaiss M, Bachert P. Chemical exchange saturation transfer (CEST) and MR Z-spectroscopy *in vivo*: a review of theoretical approaches and methods. *Phys. Med. Biol.* 2013; 58: R221–69. DOI: 10.1088/0031-9155/58/22/R221.
3. Zhou J, Payen J-F, Wilson DA, Traystman RJ, van Zijl PCM. Using the amide proton signals of intracellular proteins and peptides to detect pH effects in MRI. *Nat. Med.* 2003; 9: 1085–1090. DOI: 10.1038/nm907.
4. Kogan F, Haris M, Singh A, Cai K, Debrosse C, Nanga RPR, Hariharan H, Reddy R. Method for high-resolution imaging of creatine *in vivo* using chemical exchange saturation transfer. *Magn. Reson. Med.* 2014; 71: 164–172. DOI: 10.1002/mrm.24641.
5. Zu Z, Spear J, Li H, Xu J, Gore JC. Measurement of regional cerebral glucose uptake by magnetic resonance spin-lock imaging. *Magn. Reson. Imaging* 2014; 32: 1078–1084. DOI: 10.1016/j.mri.2014.06.002.
6. Zhang S, Merritt M, Woessner DE, Lenkinski RE, Sherry AD. PARACEST agents: modulating MRI contrast via water proton exchange. *Acc. Chem. Res.* 2003; 36: 783–790. DOI: 10.1021/ar020228m.
7. Liu G, Liang Y, Bar-Shir A, Chan KWW, Galpoththawela CS, Bernard SM, Tse T, Yadav NN, Walczak P, McMahon MT, Bulte JWM, van Zijl PCM, Gilad AA. Monitoring enzyme activity using a diamagnetic chemical exchange saturation transfer magnetic resonance imaging contrast agent. *J. Am. Chem. Soc.* 2011; 133: 16326–16329. DOI: 10.1021/ja204701x.
8. Sun PZ, Farrar CT, Sorensen AG. Correction for artifacts induced by B_0 and B_1 field inhomogeneities in pH-sensitive chemical exchange-saturation transfer (CEST) imaging. *Magn. Reson. Med.* 2007; 58: 1207–1215. DOI: 10.1002/mrm.21398.
9. Jin T, Wang P, Zong X, Kim S-G. Magnetic resonance imaging of the Amine-Proton EXchange (APEX) dependent contrast. *Neuroimage* 2012; 59: 1218–1227. DOI: 10.1016/j.neuroimage.2011.08.014.
10. Zaiss M, Xu J, Goerke S, Khan IS, Singer RJ, Gore JC, Gochberg DF, Bachert P. Inverse Z-spectrum analysis for spillover-, MT-, and T1-corrected steady-state pulsed CEST-MRI – application to pH-weighted MRI of acute stroke. *NMR Biomed.* 2014; 27: 240–252. DOI: 10.1002/nbm.3054.
11. McMahon MT, Gilad AA, Zhou J, Sun PZ, Bulte JWM, van Zijl PCM. Quantifying exchange rates in CEST agents using the saturation time and saturation power dependencies of the magnetization transfer effect on the MRI signal (QUEST and QUESP): pH calibration for poly-L-lysine and a starburst dendrimer. *Magn. Reson. Med.* 2006; 55: 836–847. DOI: 10.1002/mrm.20818.
12. Sun PZ, Wang Y, Dai Z, Xiao G, Wu R. Quantitative chemical exchange saturation transfer (qCEST) MRI – RF spillover effect-corrected omega plot for simultaneous determination of labile proton fraction ratio and exchange rate. *Contrast Media Mol. Imaging* 2014; 9: 268–275. DOI: 10.1002/cmml.1569.
13. Wu R, Xiao G, Zhou IY, Ran C, Sun PZ. Quantitative chemical exchange saturation transfer (qCEST) MRI – omega plot analysis of RF-spillover-corrected inverse CEST ratio asymmetry for simultaneous determination of labile proton ratio and exchange rate. *NMR Biomed.* 2015; 28: 376–383. DOI: 10.1002/nbm.3257.
14. Kunth M, Witte C, Schröder L. Quantitative chemical exchange saturation transfer with hyperpolarized nuclei (qHyper-CEST): sensing xenon-host exchange dynamics and binding affinities by NMR. *J. Chem. Phys.* 2014; 141: 194202. DOI: 10.1063/1.4901429.
15. Tee YK, Harston GWJ, Blockley N, Okell TW, Levman J, Sheerin F, Cellerini M, Jezzard P, Kennedy J, Payne SJ, Chappell MA. Comparing different analysis methods for quantifying the MRI amide proton

- transfer (APT) effect in hyperacute stroke patients. *NMR Biomed.* 2014; 27: 1019–1029. DOI: 10.1002/nbm.3147.
16. Helmlinger G, Yuan F, Dellian M, Jain RK. Interstitial pH and pO_2 gradients in solid tumors *in vivo*: high-resolution measurements reveal a lack of correlation. *Nat. Med.* 1997; 3: 177–182. DOI: 10.1038/nm0297-177.
17. Radbruch A, Lutz K, Wiestler B, Bäumer P, Heiland S, Wick W, Bendszus M. Relevance of T2 signal changes in the assessment of progression of glioblastoma according to the Response Assessment in Neurooncology criteria. *Neuro Oncol.* 2012; 14: 222–229. DOI: 10.1093/neuonc/nor200.
18. Lutz K, Wiestler B, Graf M, Bäumer P, Floca R, Schlemmer H-P, Heiland S, Wick W, Bendszus M, Radbruch A. Infiltrative patterns of glioblastoma: identification of tumor progress using apparent diffusion coefficient histograms. *J. Magn. Reson. Imaging* 2014; 39: 1096–1103. DOI: 10.1002/jmri.24258.
19. Cai K, Singh A, Poptani H, Li W, Yang S, Lu Y, Hariharan H, Zhou XJ, Reddy R. CEST signal at 2 ppm (CEST@2 ppm) from Z-spectral fitting correlates with creatine distribution in brain tumor. *NMR Biomed.* 2014; 28: 1–8. DOI: 10.1002/nbm.3216.
20. Zhou J, Wilson DA, Sun PZ, Klaus JA, van Zijl PCM. Quantitative description of proton exchange processes between water and endogenous and exogenous agents for WEX, CEST, and APT experiments. *Magn. Reson. Med.* 2004; 51: 945–952. DOI: 10.1002/mrm.20048.
21. Zaiss M, Schmitt B, Bachert P. Quantitative separation of CEST effect from magnetization transfer and spillover effects by Lorentzian-line-fit analysis of z-spectra. *J. Magn. Reson.* 2011; 211: 149–155. DOI: 10.1016/j.jmr.2011.05.001.
22. Sun PZ. Simplified quantification of labile proton concentration-weighted chemical exchange rate (k_{ws}) with RF saturation time dependent ratiometric analysis (QUESTRA). *Magn. Reson. Med.* 2012; 67: 936–942. DOI: 10.1002/mrm.23068.
23. Sun PZ, Benner T, Kumar A, Sorensen AG. Investigation of optimizing and translating pH-sensitive pulsed-chemical exchange saturation transfer (CEST) imaging to a 3 T clinical scanner. *Magn. Reson. Med.* 2008; 60: 834–841. DOI: 10.1002/mrm.21714.
24. Zu Z, Li K, Janve VA, Does MD, Gochberg DF. Optimizing pulsed-chemical exchange saturation transfer imaging sequences. *Magn. Reson. Med.* 2011; 66: 1100–1108. DOI: 10.1002/mrm.22884.
25. Dixon W, Ren J, Lubag A, Ratnakar J, Vinogradov E, Hancu I, Lenkinski R, Sherry A. A concentration independent method to measure exchange rates in PARACEST agents. *Magn. Reson. Med.* 2010; 63: 625–632. DOI: 10.1002/mrm.22242.A.
26. Sun PZ, Xiao G, Wu R. Simplified simultaneous determination of CEST agent concentration and exchange rate. *Proc. Int. Soc. Mag. Reson. Med.* 2014; 22: 3306.
27. Zaiss M, Bachert P. Exchange-dependent relaxation in the rotating frame for slow and intermediate exchange – modeling off-resonant spin-lock and chemical exchange saturation transfer. *NMR Biomed.* 2013; 26: 507–518. DOI: 10.1002/nbm.2887.
28. McConnell HM. Reaction rates by nuclear magnetic resonance. *J. Chem. Phys.* 1958; 28: 430. DOI: 10.1063/1.1744152.
29. Roeloffs V, Meyer C, Bachert P, Zaiss M. Towards quantification of pulsed spinlock and CEST at clinical MR scanners: an analytical interleaved saturation-relaxation (ISAR) approach. *NMR Biomed.* 2014; 28: 40–53. DOI: 10.1002/nbm.3192.
30. Santyr GE, Fairbanks EJ, Kelcz F, Sorenson JA. Off-resonance spin locking for MR imaging. *Magn. Reson. Med.* 1994; 32: 43–51. DOI: 10.1002/mrm.1910320107.
31. Goerke S, Zaiss M, Bachert P. Characterization of creatine guanidinium proton exchange by water-exchange (WEX) spectroscopy for absolute-pH CEST imaging *in vitro*. *NMR Biomed.* 2014; 27: 507–518. DOI: 10.1002/nbm.3086.
32. Schmitt B, Zaiss M, Zhou J, Bachert P. Optimization of pulse train presaturation for CEST imaging in clinical scanners. *Magn. Reson. Med.* 2011; 65: 1620–1629. DOI: 10.1002/mrm.22750.
33. Kim M, Gillen J, Landman BA, Zhou J, van Zijl PCM. Water saturation shift referencing (WASSR) for chemical exchange saturation transfer (CEST) experiments. *Magn. Reson. Med.* 2009; 61: 1441–1450. DOI: 10.1002/mrm.21873.Water.
34. Windschuh J, Zaiss M, Meissner J-E, Paech D, Radbruch A, Ladd ME, Bachert P. Correction of B1-inhomogeneities for relaxation-compensated CEST imaging at 7 T. *NMR Biomed.* 2015; 28: 529–537. DOI: 10.1002/nbm.3283.
35. Lourakis MIA. *levmar: Levenberg–Marquardt Nonlinear Least Squares Algorithms in C/C++*. 2004 <http://users.ics.forth.gr/~lourakis/levmar/>.
36. Haris M, Nanga RPR, Singh A, Cai K, Kogan F, Hariharan H, Reddy R. Exchange rates of creatine kinase metabolites: feasibility of imaging creatine by chemical exchange saturation transfer MRI. *NMR Biomed.* 2012; 25: 1305–1309. DOI: 10.1002/nbm.2792.
37. Liepinsh E, Otting G. Proton exchange rates from amino acid side chains – implications for image contrast. *Magn. Reson. Med.* 1996; 35: 30–42. DOI: 10.1002/mrm.1910350106.
38. Trott O, Palmer AG. $R_{1\rho}$ relaxation outside of the fast-exchange limit. *J. Magn. Reson.* 2002; 154: 157–160. DOI: 10.1006/jmre.2001.2466.
39. Mangia S, Liimatainen T, Garwood M, Michaeli S. Rotating frame relaxation during adiabatic pulses vs. conventional spin lock: simulations and experimental results at 4 T. *Magn. Reson. Imaging* 2009; 27: 1074–1087. DOI: 10.1016/j.jmr.2009.05.023.
40. Zu Z, Janve VA, Xu J, Does MD, Gore JC, Gochberg DF. A new method for detecting exchanging amide protons using chemical exchange rotation transfer. *Magn. Reson. Med.* 2013; 69: 637–647. DOI: 10.1002/mrm.24284.
41. Jin T, Autio J, Obata T, Kim S-G. Spin-locking versus chemical exchange saturation transfer MRI for investigating chemical exchange process between water and labile metabolite protons. *Magn. Reson. Med.* 2011; 65: 1448–1460. DOI: 10.1002/mrm.22721.
42. Zu Z, Xu J, Li H, Chekmenev EY, Quarles CC, Does MD, Gore JC, Gochberg DF. Imaging amide proton transfer and nuclear Overhauser enhancement using chemical exchange rotation transfer (CERT). *Magn. Reson. Med.* 2014; 72: 471–476. DOI: 10.1002/mrm.24953.
43. Xu J, Yadav NN, Bar-Shir A, Jones CK, Chan KKY, Zhang J, Walczak P, McMahon MT, van Zijl PCM. Variable delay multi-pulse train for fast chemical exchange saturation transfer and relayed-nuclear Overhauser enhancement MRI. *Magn. Reson. Med.* 2014; 71: 1798–1812. DOI: 10.1002/mrm.24850.
44. Meissner J-E, Windschuh J, Zaiss M, Paech D, Radbruch A, Bachert P. Multi-pool CEST imaging of glioblastoma at 7 T. *Proc. Int. Soc. Mag. Reson. Med.* 2014; 22: 3152.
45. Jones CK, Huang A, Xu J, Edden RAE, Schär M, Hua J, Oskolkov N, Zaca D, Zhou J, McMahon MT, Pillai JJ, van Zijl PCM. Nuclear Overhauser enhancement (NOE) imaging in the human brain at 7 T. *Neuroimage* 2013; 77: 114–124. DOI: 10.1016/j.neuroimage.2013.03.047.
46. Desmond KL, Moosvi F, Stanis GJ. Mapping of amide, amine, and aliphatic peaks in the CEST spectra of murine xenografts at 7 T. *Magn. Reson. Med.* 2013; 71: 1841–1853. DOI: 10.1002/mrm.24822.
47. Singh A, Cai K, Haris M, Hariharan H, Reddy R. On B₁ inhomogeneity correction of *in vivo* human brain glutamate chemical exchange saturation transfer contrast at 7 T. *Magn. Reson. Med.* 2013; 69: 818–824. DOI: 10.1002/mrm.24290.
48. Henkelman RM, Stanis GJ, Graham SJ. Magnetization transfer in MRI: a review. *NMR Biomed.* 2001; 14: 57–64. DOI: 10.1002/nbm.683.
49. Zaiss M, Zu Z, Xu J, Schuenke P, Gochberg DF, Gore JC, Ladd ME, Bachert P. A combined analytical solution for chemical exchange saturation transfer and semi-solid magnetization transfer. *NMR Biomed.* 2015; 28: 217–230. DOI: 10.1002/nbm.3237.
50. Heo H-Y, Zhang Y, Lee D-H, Hong X, Zhou J. Quantitative assessment of amide proton transfer (APT) and nuclear Overhauser enhancement (NOE) imaging with extrapolated semi-solid magnetization transfer reference (EMR) signals: application to a rat glioma model at 4.7 Tesla. *Magn. Reson. Med.* 2015. DOI: 10.1002/mrm.25581.
51. Xu J, Zaiss M, Zu Z, Li H, Xie J, Gochberg DF, Bachert P, Gore JC. On the origins of chemical exchange saturation transfer (CEST) contrast in tumors at 9.4 T. *NMR Biomed.* 2014; 27: 406–416. DOI: 10.1002/nbm.3075.
52. Friedman JI, Xia D, Regatte RR, Jerschow A. Transfer rate edited experiment for the selective detection of chemical exchange via saturation transfer (TRE-CEST). *J. Magn. Reson.* 2015; 256: 43–51. DOI: 10.1016/j.jmr.2015.04.010.

SUPPORTING INFORMATION

Additional supporting information may be found in the online version of this article at the publisher's web-site.

APPENDIX

Appendix A1. Derivation of AREX in the pulsed case

The normalized steady-state magnetization in the case of pulsed pre-saturation is given by

$$Z_{\text{pulsed}}^{\text{SS}} = \frac{(1 - e^{-R_{1A}t_d}) - \frac{\cos(\theta)R_{1A}}{R_{1p}(\Delta\omega)}(1 - e^{R_{1p}(\Delta\omega)t_p})}{e^{R_{1p}(\Delta\omega)t_p} - e^{-R_{1A}t_d}}. \quad (\text{A1})$$

Using the assumption $\exp(x) \approx 1 + x$ leads to

$$Z_{\text{pulsed}}^{\text{SS}} = \frac{(1 - (1 - R_{1A}t_d)) - \frac{\cos(\theta)R_{1A}}{R_{1p}}(1 - (1 + R_{1p}t_p))}{(1 + R_{1p}t_p) - (1 - R_{1A}t_d)} \quad (\text{A2})$$

$$\approx \frac{R_{1A}\left(\frac{t_d}{t_p} + \cos(\theta)\right)}{R_{1p} + R_{1A}\frac{t_d}{t_p}}. \quad (\text{A3})$$

Introducing the duty cycle $\text{DC} = t_p/t_p + t_d$ results in

$$Z_{\text{pulsed}}^{\text{SS}} \approx \frac{R_{1A}(1 - \text{DC} + \text{DC} \cdot \cos(\theta))}{R_{1p}\text{DC} + R_{1A}(1 - \text{DC})}. \quad (\text{A4})$$

Considering only small flip angles θ , the cosine term will be approximately one, and with

$$\text{MTR}_{\text{Rex}} = \frac{1}{Z_{\text{lab}}} - \frac{1}{Z_{\text{ref}}} \quad (\text{A5})$$

yields

$$\text{MTR}_{\text{Rex}} = \frac{1}{\frac{R_{1A}}{R_{1,\text{lab}}\text{DC} + R_{1A}(1 - \text{DC})}} - \frac{1}{\frac{R_{1A}}{R_{1,\text{ref}}\text{DC} + R_{1A}(1 - \text{DC})}} \quad (\text{A6})$$

$$= \frac{\text{DC}(R_{1,\text{lab}} - R_{1,\text{ref}})}{R_{1A}}. \quad (\text{A7})$$

Using the definition of $R_{1,\text{lab}} = R_{\text{eff}} + R_{\text{ex}}$ and $R_{1,\text{ref}} = R_{\text{eff}}$, it follows that

$$\text{MTR}_{\text{Rex}} = \frac{R_{\text{ex}}\text{DC}}{R_{1A}}. \quad (\text{A8})$$

Multiplication by R_{1A} yields the definition of AREX as defined in (10):

$$\text{AREX} = \text{MTR}_{\text{Rex}}R_{1A} = R_{\text{ex}}\text{DC}. \quad (\text{A9})$$

Appendix A2. Derivation of the time-dependent R_{1p} for Gaussian-shaped pulses

For shaped pulses, a time dependent R_{1p} has to be considered:

$$R_{1p}(\omega(t)) = R_{\text{eff}}(\omega(t)) + R_{\text{ex}}(\omega(t)). \quad (\text{A10})$$

Integration as a function of time leads to an average R_{1p} :

$$\overline{R_{1p}} = \frac{1}{t_p} \int_0^{t_p} R_{\text{eff}}(\omega(t))dt + \frac{1}{t_p} \int_0^{t_p} R_{\text{ex}}(\omega(t))dt \quad (\text{A11})$$

$$= \frac{1}{t_p} \int_0^{t_p} \left[R_{1A} + (R_{2A} - R_{1A}) \frac{\omega_1^2(t)}{\omega_1^2(t) + \Delta\omega} \right] dt + \frac{1}{t_p} \int_0^{t_p} f_B k_{BA} \frac{\omega_1^2(t)}{\omega_1^2(t) + k_{BA}(k_{BA} + R_{2B})} dt \quad (\text{A12})$$

Rearranging yields

$$\overline{R_{1p}} = R_{1A} + \frac{(R_{2A} - R_{1A})}{t_p} \int_0^{t_p} \frac{\omega_1^2(t)}{\Delta\omega} \cdot \frac{1}{\frac{\omega_1^2(t)}{\Delta\omega^2} + 1} dt + \frac{f_B k_{BA}}{t_p} \int_0^{t_p} \frac{\omega_1^2(t)}{k_{BA}(k_{BA} + R_{2B})} \cdot \frac{1}{\frac{\omega_1^2(t)}{k_{BA}(k_{BA} + R_{2B})} + 1} dt \quad (\text{A13})$$

Substitution with $x^2 = \frac{1}{\Delta\omega^2}$ and $y^2 = \frac{1}{k_{BA}(k_{BA} + R_{2B})}$ leads to

$$\overline{R_{1p}} = R_{1A} + \frac{(R_{2A} - R_{1A})}{t_p} \int_0^{t_p} \omega_1^2(t)x^2 \cdot \frac{1}{\omega_1^2(t)x^2 + 1} dt + \frac{f_B k_{BA}}{t_p} \int_0^{t_p} \omega_1^2(t)y^2 \cdot \frac{1}{\omega_1^2(t)y^2 + 1} dt \quad (\text{A14})$$

This integral can be solved numerically. However, in the following we show an analytical approximation.

Analytical integration

Due to the same form of the integrals in Equation [A14], calculations can be performed for x^2 and transferred to y^2 . Employing the power-series of $1/(x^2 + 1)$, the integral can be rewritten as

$$\frac{1}{t_p} \int_0^{t_p} \omega_1^2(t)x^2 \cdot \frac{1}{\omega_1^2(t)x^2 + 1} dt = \frac{1}{t_p} \int_0^{t_p} \omega_1^2(t)x^2 \cdot \left(\sum_{l=0}^{\infty} (-\omega_1^2(t)x^2)^l \right) dt \quad (\text{A15})$$

$$= \frac{1}{t_p} \int_0^{t_p} \left(- \sum_{l=1}^{\infty} (-\omega_1^2(t)x^2)^l \right) dt \quad (\text{A16})$$

Assuming a Gaussian-shaped pulse defined by

$$\omega_1(t) = \omega_1 t_p \frac{1}{\sigma\sqrt{2\pi}} \cdot e^{-\left(\frac{t-t_p/2}{\sigma}\right)^2} \quad (\text{A17})$$

with

$$\int_0^{t_p} \frac{\omega_1(t)}{t_p} dt = \omega_1 \quad (\text{A18})$$

and the n th moments of ω_1 ,

$$\int \omega_1^n dt = \int \left(\omega_1 t_p \frac{1}{\sigma\sqrt{2\pi}} e^{-\left(\frac{t-t_p/2}{\sigma}\right)^2} \right)^n dt = (\omega_1 t_p)^n \left(\frac{1}{\sigma\sqrt{2\pi}} \right)^{n-1} \frac{1}{\sqrt{n}} \quad (\text{A19})$$

every single term of the infinite series can be analytically integrated and yields

$$\frac{1}{t_p} \int_0^{t_p} \left(- \sum_{l=1}^{\infty} (-\omega_1^2(t)x^2)^l \right) dt = - \frac{1}{t_p} \sum_{l=1}^{\infty} \left(-\omega_1^2 t_p^2 x^2 \right)^l \left(\frac{1}{\sigma\sqrt{2\pi}} \right)^{2l-1} \cdot \frac{1}{\sqrt{2l}} \quad (\text{A20})$$

$$:= \psi(-\omega_1^2(t)x^2, \sigma, t_p).$$

The function $\psi(X, \sigma, t_p)$ is defined by the power series as given in Appendix A3. By inserting Equation [A20] into Equation [A14], an analytic expression for $\overline{R_{1p}}$ can be derived:

$$\overline{R_{1p}} = R_{1A} + (R_{2A} - R_{1A}) \cdot \psi(-\omega_1^2(t)x^2, \sigma, t_p) + f_B k_{BA} \times \psi(-\omega_1^2(t)y^2, \sigma, t_p) \quad (A21)$$

However, the linearity of the Ω -plots in the case of pulsed pre-saturation (Figs. 1, 2, and 4) indicates that R_{ex} and thus $\psi(X, \sigma, t_p)$ must have the shape $X^2/(1+X^2)$. This is the case if $X < 1$, as given in Appendix A3. Then Equation [A21] simplifies to

$$\overline{R_{1p}} \approx R_{1A} + (R_{2A} - R_{1A}) \times c_1 \frac{\omega_1^2 \cdot x^2}{\omega_1^2 \cdot x^2 + c_2^2} + f_B k_{BA} \times c_1 \frac{\omega_1^2 \cdot y^2}{\omega_1^2 \cdot y^2 + c_2^2} \quad (A22)$$

With the form factors $c_1 = \sqrt{2\pi} \sigma / t_p$ and $c_2 = c_1 \cdot \sqrt[4]{2} = \sqrt{2\pi} \sigma / t_p \cdot \sqrt[4]{2}$, substitution of $x^2 = \frac{1}{\Delta\omega^2}$ and $y^2 = \frac{1}{k_{BA}(k_{BA} + R_{2B})}$ yields

$$\overline{R_{1p}} \approx R_{1A} + (R_{2A} - R_{1A}) \cdot c_1 \frac{\omega_1^2}{\omega_1^2 + \Delta\omega^2 \cdot c_2^2} + f_B k_{BA} \times c_1 \frac{\omega_1^2}{\omega_1^2 + k_{BA}(k_{BA} + R_{2B}) \cdot c_2^2} \quad (A23)$$

Thus, AREX in the case of a pulsed pre-saturation is modified to

$$\text{AREX}_{\text{pulsed}} = \text{DC} \cdot f_B k_{BA} \cdot c_1 \cdot \frac{\omega_1^2}{\omega_1^2 + k_{BA}(k_{BA} + R_{2B}) \cdot c_2^2} \quad (A24)$$

which yields a linear equation of the form $1/\text{AREX} = m \cdot 1/\omega_1^2 + n$:

$$\frac{1}{\text{AREX}_{\text{pulsed}}} = \frac{(k_{BA} + R_{2B})c_2^2}{f_B \cdot \text{DC} \cdot c_1} \cdot \frac{1}{\omega_1^2} + \frac{1}{f_B k_{BA} \cdot \text{DC} \cdot c_1} \quad (A25)$$

Determination of the slope m and y-intersection n enables quantification of f_B and k_{BA} in the case of Gaussian-shaped saturation:

$$f_B^{\text{shaped-pulses}} = \frac{1}{c_1 \cdot \text{DC} \cdot n \cdot \left(-\frac{R_{2B}}{2} + \sqrt{\frac{R_{2B}^2}{4} + \frac{m}{n \cdot c_2^2}} \right)} \quad (A26)$$

$$k_{BA}^{\text{shaped-pulses}} = -\frac{R_{2B}}{2} + \sqrt{\frac{R_{2B}^2}{4} + \frac{m}{n \cdot c_2^2}} \quad (A27)$$

Appendix A3. The power of series $\psi(X, \sigma, t_p)$

The found power series $\psi(X, \sigma, t_p)$ (Equation [A20]) is generally defined as

$$\psi(X, \sigma, t_p) = -\frac{1}{t_p} \sum_{l=1}^{\infty} X^l \left(\frac{1}{\sigma\sqrt{2\pi}} \right)^{2l-1} \cdot \frac{t_p^2}{\sqrt{2l}} \quad (A28)$$

If $X < 1$, this series can be transformed to the geometric series using the approximation $\sqrt{2l} \approx \sqrt{2}$. This yields a geometric series $G(X, \sigma, t_p)$, which agrees with $\psi(X, \sigma, t_p)$ to second order:

$$\psi(X, \sigma, t_p) \approx G(X, \sigma, t_p) = -\frac{\sigma\sqrt{2\pi}}{t_p} \cdot \sum_{l=1}^{\infty} \left(X \left(\frac{t_p}{\sigma\sqrt{2\pi}} \right)^2 \cdot \frac{1}{\sqrt{2}} \right)^l = -\frac{\sigma\sqrt{2\pi}}{t_p} \cdot \sum_{l=1}^{\infty} (q)^l \quad (A29)$$

This yields a closed form if $q < 1$:

$$G(X, \sigma, t_p) = -\frac{\sigma\sqrt{2\pi}}{t_p} \frac{q}{1-q} = -\frac{\sigma\sqrt{2\pi}}{t_p} \frac{X \cdot \left(\frac{t_p}{\sigma\sqrt{2\pi}} \right)^2 \cdot \frac{1}{\sqrt{2}}}{1 - X \cdot \left(\frac{t_p}{\sigma\sqrt{2\pi}} \right)^2 \cdot \frac{1}{\sqrt{2}}} \quad (A30)$$

Rearranging leads to

$$G(X, \sigma, t_p) = \frac{\sigma\sqrt{2\pi}}{t_p} \frac{X}{X - \left(\frac{\sigma\sqrt{2\pi}}{t_p} \right)^2 \cdot \sqrt{2}} \quad (A31)$$

Introducing the form factors $c_1 = \sqrt{2\pi} \sigma / t_p$ and $c_2 = c_1 \cdot \sqrt[4]{2} = \sqrt{2\pi} \sigma / t_p \cdot \sqrt[4]{2}$ yields

$$\psi(X, \sigma, t_p) \approx G(X, \sigma, t_p) = c_1 \frac{X}{X - c_2^2} \quad (A32)$$